



Effective redox reaction in a three-body smart photocatalyst through multi-interface modulation of organic semiconductor junctioned with metal and inorganic semiconductor



Farzin Nekouei ^{a,*}, Tianyi Wang ^b, Farzaneh Keshtpour ^c, Yun Liu ^a, Hao Li ^b, Shahram Nekouei ^d

^a Research School of Chemistry, The Australian National University, ACT, 2601, Australia

^b Advanced Institute for Materials Research (WPI-AIMR), Tohoku University, Sendai 980-8577, Japan

^c Young Researchers and Elite Club, Central Tehran Branch, Islamic Azad University, Tehran, Iran

^d Young Researchers and Elite Club, Science and Research Branch, Islamic Azad University, Tehran, Iran

ARTICLE INFO

Keywords:

Hydrogen evolution
Selective oxidation
Multi-interface photocatalyst
S-scheme heterojunction

ABSTRACT

Forming metal/semiconductor heterojunctions is a well-known strategy to enhance photo-reaction through interface band bending. However, challenges remain in simultaneously minimizing fast charge carrier recombination and avoiding potential photo-corrosion in photocatalysts for high efficiency and long lifetime application in energy, environment, and green chemistry. We here design and propose a new strategy by which multi-interface band structure modulation occurs in a three-body photocatalyst, exemplified by Ag/PDA@Ag₂S (PDA: polydopamine). Experimental analyses including *in-situ* x-ray photoelectron spectroscopy (XPS) and time-resolved photoluminescence (TRPL) spectroscopy together with projected density of states studies suggest an S-scheme heterojunction formation in the PDA@Ag₂S, which greatly enhances the separation of photogenerated carriers. Consequently, we demonstrate that this multibody photocatalyst exhibits superior stability and selective oxidation of a series of ionic dyes under solar-simulated irradiation. The hydrogen generation efficiency (reduction) is also remarkably enhanced compared to virgin Ag/Ag₂S photocatalysts. We believe this work brings a new insight into catalyst design.

1. Introduction

Over the past few decades, the growth of the world population along with rapid industrialization and fossil fuels depletion, the imminent crisis of energy and natural resources as well as environmental deterioration have impelled researchers to find solutions and tackle the issues for a sustainable future [1–3]. Smart, stable, and selective photocatalytic processes are of great interest in various fields but their creation and control have remained an unmet challenge. Additionally, photocatalytic processes powered by solar energy are considered a promising solution to the current energy and environmental deterioration crises [4]. Nonetheless, due to fast charge carrier recombination of photogenerated carriers and low selectivity, photocatalysis processes remain unsatisfactory [5]. A great amount of effort has been spent on the rational design of photocatalysts through developing different strategies including different heterojunction construction [6], defect formation [7], functionalized materials [8], incorporating cocatalysts [9], and

structural engineering [10]. Modulating work functions and energy levels of semiconductors is also regarded as an alternative strategy to suppress the recombination of the photogenerated carriers. Energy level manipulation to date has been limited to the surface Fermi level and band bending on nanostructured heterojunction photocatalysts, such as the metal/semiconductor heterojunction [10]. In terms of classical semiconductor physics [11], either the electron depletion or accumulation layer is formed at the interface due to the joint contribution arising from the Fermi level alignment and the work function difference of the metal and semiconductor.

For this purpose, Ag₂S/Ag nanohybrids—one of the important Semiconductor/Metal heterostructures—were selected as an origin two-body system for testing. Due to its high optical absorption coefficient, chemical stability, and efficient photoluminescence [12], it has been used as a photocatalyst [13,14], IR detector [15], photoconductor [16], and bioimaging agent [17] originating from unique properties of Ag₂S. On the other hand, such a ~ 1 eV narrow band gap of Ag₂S will bring

* Corresponding author.

E-mail addresses: Farzin.nekouei@anu.edu.au, F.nekouei@hotmail.com (F. Nekouei).

serious issues caused by potential photo-corrosion under the irradiation of different lights [18]. The work function of Ag and the bottom of the conduction band of Ag_2S are -4.26 and -4.42 eV from the vacuum energy level. When Ag comes into contact with Ag_2S , electrons from the Ag with higher energy (lower work function) can move into the Ag_2S . In the Ag_2S , an equal number of holes are left behind, creating a region with excess positive charge (holes) near the interface. As electrons move from the Ag to the Ag_2S , an electric field is established at the interface, preventing further electron flow. This electric field creates a built-in potential across the junction, known as the built-in potential or potential barrier. Thus, the holes are not able to transfer to the Ag side because of the energy barrier. Hence, its photocatalytic performance would be restricted by partially favourable band bending and photogenerated charge carrier separation as well as serious self-photo corrosion caused by the reduction of lattice Ag^+ into metallic Ag. Heterostructure photocatalysts obtained by combining different semiconductor materials have conferred new properties, for example, higher selectivity, stability, and charge separation [19]. Organic semiconductor–metal interfaces are well-known in organic electronics, typically serving to either inject or extract charges from an organic semiconductor film [20].

Here, we take a step towards this goal in combination with selectivity and stability enhancement using interface phenomena of PDA junctioned with Ag and Ag_2S via a ternary plasmonic metal–organic semiconductor–inorganic semiconductor system. TRPL and in-situ XPS analyses supported by PDOS studies revealed charge transfer facilitation via an S-scheme heterojunction at the PDA and Ag_2S interface accompanying promising new properties for the Ag/PDA@ Ag_2S smart heterojunction as a bifunctional photocatalyst. We report surface charge switchable and pH-responsive Ag/PDA@ Ag_2S heterointerfaces as smart photocatalysts for selective oxidation of cationic and ionic organic dyes and enhanced hydrogen evolution under solar light irradiation.

2. Experimental and calculation

2.1. Computational methods

Spin-polarized density functional theory (DFT) was used to analyze the structures via the Vienna Ab-initio Simulation Package 6.4.1 (VASP) [21]. The electron correlation function was modified with the

generalized gradient approximation (GGA) method with the Perdew-Burke-Ernzerhof (PBE) functional [22]. The projected augmented-wave method was applied to describe core electrons, and Kohn-Sham wave functions were used to describe the valence electrons [23,24]. The kinetic energy cutoff was 400 eV, and the Monkhorst-Pack method with the k -point mesh ($3 \times 3 \times 1$) was utilized to sample the Brillouin zone [25]. A 15 Å vacuum space was set to avoid the interaction of neighboring layers. All atoms were fully relaxed when the residual force was lower than 0.03 eV/Å. The optimized configuration of PDA-Ag₂S is illustrated in Figure S1.

2.2. Materials

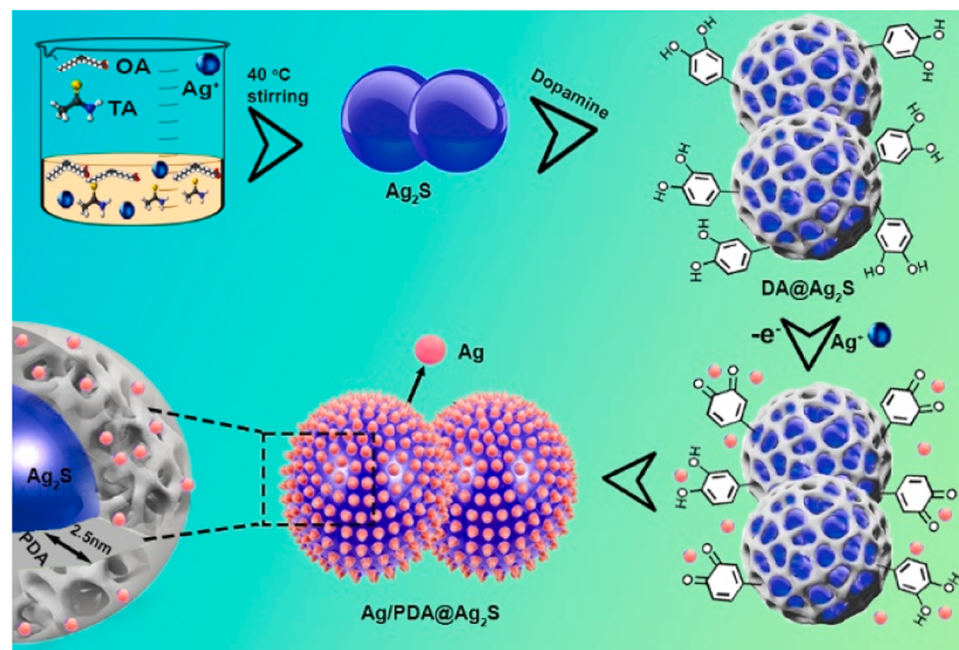
All reagents used in this study were purchased from Sigma-Aldrich Co. without further purification and listed in Supporting Information (SI), entitled S1.

2.3. Preparation of Ag/PDA@ Ag_2S

Another important property of PDA polymerization is its reducing ability toward metal ions allowing the preparation of metal nanocomposites using direct route. Thus, an additional reductant is not required in some metal NPs/composite syntheses in association with the polymerization process of dopamine (DA). Ag NPs anchored on the surface of PDA@ Ag_2S core/shell microstructural composites supported via a fast procedure method as illustrated in Scheme 1. The procedure is explained in detail and given in SI as S2.

2.4. Instruments

X-ray diffraction (XRD) spectra were obtained using a Bruker AXS-D8 Advance model system. The diffracted intensity of Cu K α radiation (0.154 nm, 40 kV, and 40 mA) was measured over a 20 range between 20 and 80°. The field emission scanning electron microscopy (FESEM) was performed on Zeiss Supra, model 55VP, Germany. Transmission electron microscopy (TEM) and high-resolution TEM images were obtained by (JEOL JEM-2010). A double-beam spectrophotometer (Carry 5000 UV-Vis-NIR, Varian) was used for the determination of the concentration of dyes. Fourier transform infrared spectroscopy (FT-IR)



Scheme 1. A schematic illustration of the formation of the Ag/PDA@ Ag_2S smart heterojunction photocatalyst.

equipped with an attenuated total reflectance accessory configured with a KSR-5 crystal (ATR, PerkinElmer) was used for recording IR spectra in the region 4000–400 cm⁻¹ at room temperature. X-ray photoelectron spectroscopic (XPS) measurements were performed using a Thermo Escalab 250 with a monochromated Al-K α excitation source. The Electron spin resonance (ESR) signals of radicals were recorded using a Bruker A300-10/12/S-LC spectrometer that 2-methyl-N-(4-pyridinylmethylene)-2-propanamine N,N'-dioxide (POBN) was used as a spin trap for tracking H radicals. Electro-kinetic potentials of the PDA-coated Ag/Ag₂S hybrid composite as aqueous suspensions were acquired with ZetaPlus4 Brookhaven zeta-potential analyzer. Steady-state emission spectra were collected by exciting the samples at 470 nm with a PerkinElmer Lambda 35 spectrometer. The time-resolved photoluminescence (TRPL) decay spectra were probed at the excitation wavelength of 405 nm on an Edinburgh FLS 980 fluorescence spectrometer. Nitrogen adsorption–desorption isotherm surface area measurements were carried out by a specific surface area analyzer (Quantachrome Autosorb-iQ-2MP). The measurement of transient photocurrent response and electrochemical impedance spectroscopy (EIS) were conducted on a CHI660E electrochemical workstation. The electrochemical system consisted of an FTO glass covered by the photocatalyst, a Pt wire, and a saturated Ag/AgCl/KCl (saturated) electrode as the working, counter, and reference electrode, respectively. A 0.3 mol/L Na₂SO₄ aqueous solution served as the electrolyte. The SPEIS (staircase potential EIS) measurement was conducted with an AC applied voltage of 5 mV. The EIS of the active material (depending on the working electrode) varied between 0.2 to –0.6 V at a potential difference of 20 mV in a staircase behavior.

2.5. Photocatalytic activity toward dye degradation probe

To assess the photocatalytic oxidation performance of synthesised catalysts, first, 50 mg of the photocatalyst was added to 200 mL of a mixture of four cationic and anionic dye solutions (concentration of dye in water: 50 mg/L). Tris buffer solution was used to control the pH of the solution. The dye solution contained in the photocatalyst was stirred for 30 min to eliminate the effect of adsorption and reach a homogeneous mixture before the oxidation process. Subsequently, under a constant stirring condition and illumination (300 W Xe lamp equipped with AM 1.5 filter) at room temperature, each time 1 mL of liquid samples was withdrawn from the solution, filtered, and diluted at different time intervals. Finally, they were transferred into a quartz cuvette, and the absorption spectra of the samples were recorded using UV–Vis spectroscopy at relevant wavelengths. To avoid adsorption impact, all stock solutions were stirred in dark conditions for 30 min before irradiation. Upon irradiation, the absorption spectra of the samples were recorded at different time intervals using UV–Vis spectroscopy at 664, 556, 460, and 495 nm for MB, RB, MO, and CR, respectively at pH=10. At pH=2, although MB and RB had almost the same maximum wavelengths as those at pH=10, CR and MO had different wavelengths of 575 and 505 nm, respectively. Two pH values of 10 and 2 were chosen as representatives of acidic and basic mediums to probe the selectivity of the photocatalyst.

2.6. Photocatalytic hydrogen evolution activity

The photocatalytic activity of Ag/PDA@Ag₂S smart heterojunctions photocatalyst was investigated by producing H₂ from water under simulated sunlight irradiation by a 300 W Xe lamp equipped with AM 1.5 filter. 20 mg of the photocatalyst was dispersed thoroughly in bidistilled water in a Pyrex reaction cell and bubbled with nitrogen for 30 min to reach an anaerobic condition in the reaction system. To estimate the H₂ evolution efficiency of photocatalysts, we performed as our previous paper [1]. 50 mL aqueous solution containing 20 V/V % CH₃OH (10 mL) as a sacrificing electron donor to react with the photoinduced hole of the valence band to prevent the photoinduced

electron-hole pairs recombination. Before each experiment, the system was bubbled with nitrogen for 30 min to eliminate the dissolved oxygen. The evolved gases were measured by sampling 0.5 mL of evolved gas and analyzing them using online gas chromatography with a thermal conductivity Detector (TCD) and nitrogen carrier gas.

3. Results and discussion

3.1. Characterization of materials

Phase and crystal structure analysis of fabricated catalysts are presented in Fig. 1a, where the diffraction peaks of Ag₂S (●) are attributed to the space group of *P 1 21/n 1*, and the rest of the diffraction peaks, belong to the face-centered cubic Ag with a space group of *Fm* $\bar{3}$ *m*. It is noted that Ag shows a preferred orientation at (200) lattice plane. The Ag/PDA@Ag₂S pattern displays a similar x-ray diffraction (XRD) pattern as that of the bare Ag/Ag₂S, suggesting the PDA layer has no influence on Ag/Ag₂S crystalline structure that may be attributed to either the amorphous structure or ultrathin layer of the PDA, behaving like molecules, rather than molecular crystals [26,27]. Fig. 1b and S2a show scanning electron microscopy (SEM) images of both Ag/PDA@Ag₂S and bare Ag/Ag₂S, respectively. In both cases, Ag nanoparticles are anchored on the surface of either the PDA—the shell of Ag₂S, or the bare Ag₂S. Ag NPs deposited on the surface are smaller with higher uniformity when using dopamine (DA) as a reducing agent compared to NaBH₄ for Ag/Ag₂S synthesis. The average size of dumbbell-shaped Ag₂S for each loop is less than 200 nm. Inset in Fig. 1b illustrates the uniform deposition of the Ag NPs on the surface of the PDA@Ag₂S microstructure. Fig. 1c–f exhibit transmission electron microscopy (TEM) and high-resolution TEM (HRTEM) images of as-prepared photocatalysts. In Fig. 1c, a cloud-like PDA shell is evident around the Ag₂S photocatalyst. The thickness of the PDA shell is about 2.5 nm. Recent studies showed that with a less than 3 nm PDA decoration, photocatalysts' activation will not be hindered. Instead, their light absorption range can be tuned for even better photocatalytic performance.

[28,29]. HRTEM image, Fig. 1d, reveals two distinct interplanar spacing of 0.31 and 0.21 nm corresponding to the d-spacing for the (1 1 1) and (200) lattice planes of the Ag₂S and Ag, respectively. Figure S2a shows an SEM image of PDA-free Ag/Ag₂S hybrid photocatalysts indicating less uniformity of the Ag NPs on the Ag₂S. Figure S2b presents the HRTEM image of PDA-free Ag/Ag₂S showing the same lattice planes as Ag/PDA@Ag₂S. TEM images in Fig. 1e–f exhibit the separation between Ag NPs and Ag₂S particles indicating PDA acting as an interface between them. Fig. 1h–j show elemental mapping analysis of the Ag/PDA@Ag₂S, corresponding to the TEM image presented in Fig. 2g, showing clear evidence of the Ag particle's presence, which is consistent with other evidence and further confirms the construction profile of such a three-body catalyst system.

From the high-resolution X-ray photoelectron spectroscopy (XPS) spectrum of Ag3d in Figure S3b, peaks at 368.5 and 373.9 eV can be assigned to the binding energies of Ag 3d_{5/2} and Ag 3d_{3/2} of the metallic Ag⁰ which are in good agreement with previous studies [30]. It is compatible with the XRD results, confirming the existence of metallic Ag in the photocatalyst. The peaks at 367.9 and 372.9 eV would be in good agreement with Ag 3d_{5/2} and Ag 3d_{3/2} of Ag⁺ ions in the Ag₂S [31]. Figure S3f shows the XPS spectra of O1s for Ag/PDA@Ag₂S photocatalysts. The O 1 s region fits with two peaks assigned to the O=C and HO–C species. 5,6-indolequinone (C=O) is apparently dominating O 1 s region against 5,6-Dihydroxyindole (DHI). After the addition of fresh Ag⁺ ions to the PDA@Ag₂S, the spontaneous immobilization of silver can be attributed to the reducing catechol groups contained in PDA [32]. Electrons generated by the oxidation of catechol to quinone can reduce silver ions in the solution phase. More XPS results and information are presented and discussed in Figure S3. Also, Figure S4a shows Fourier transform infrared (FTIR) spectra of the Ag/PDA@Ag₂S photocatalyst.

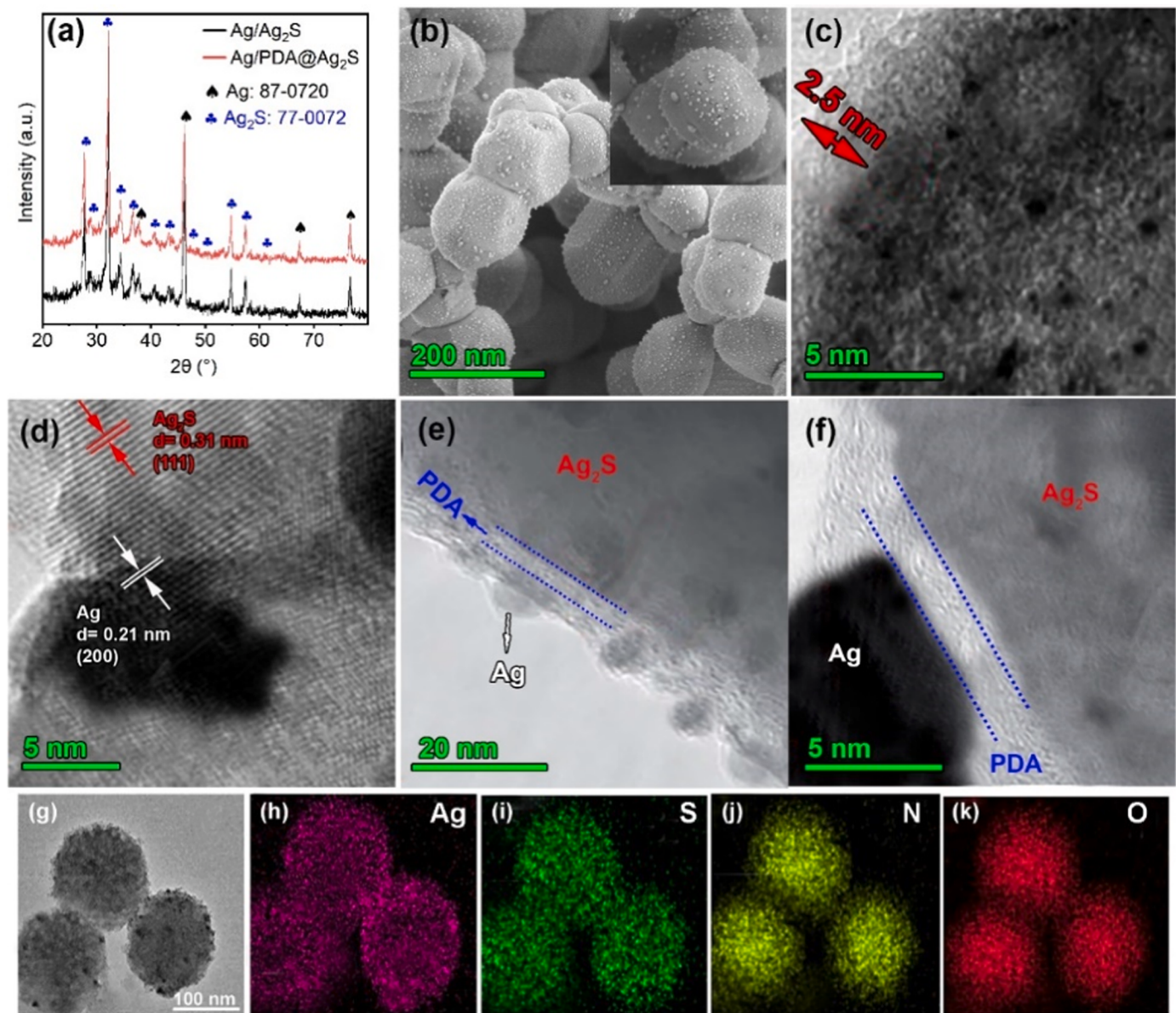


Fig. 1. (a) The XRD patterns of as-prepared Ag/Ag₂S and Ag/PDA@Ag₂S samples. (b) SEM image and (c-f) TEM images of Ag/PDA@Ag₂S. (g-k) Elemental mappings of Ag/PDA@Ag₂S.

Expect weak peaks in the region between 500 and 700 cm⁻¹ (metallic region) related to the characteristic vibration of Ag-S, the rest originate from PDA. The absorption peaks at 1515, 1620, and 3410 cm⁻¹ correspond to the shearing vibration of N-H in the amide group, aromatic rings, and -OH in catechol groups, respectively [33]. Meanwhile, the peak located at 1333 cm⁻¹ is attributed to CH₂ bending vibration. These results further prove that PDA was successfully coated on the Ag/Ag₂S cocatalyst. Figure S4b shows the Brunauer, Emmett, and Teller (BET) and pore size distribution graphs. It indicates both samples can be assigned to nitrogen adsorption-desorption isotherm type IV. Type IV isotherms indicate solids with micro- and mesopores. The Langmuir surface area was calculated at 45 and 65 m²g⁻¹ for Ag/Ag₂S and Ag/PDA@Ag₂S, respectively. The slightly higher surface area of Ag/PDA@Ag₂S can be attributed to the formation of potential pores during the Ag₂S is shelled by the PDA.

3.2. Selective oxidation of ionic dyes

To examine the selectivity and oxidative efficiency of Ag/PDA@Ag₂S

smart pH-responsive heterojunctions photocatalysts, four cationic and ionic dyes underwent photocatalysis processes. Meanwhile, the whole photodegradation tests were repeated for the Ag/Ag₂S photocatalyst as a reference. The molecular structures of used dyes including Methylene Blue (MB) and Rhodamine B (RB) as cationic dyes and Methyl Orange (MO) and Congo Red (CR) as ionic dyes are presented in Figure S5. All four dyes were separately subjected to photocatalysis processes at pH 10 and results are given in Fig. 2a and b. It is observed that the Ag/PDA@Ag₂S smart pH-responsive heterojunctions photocatalyst could successfully degrade cationic dyes with remarkably higher efficiency than anionic dyes. As discussed previously, by adjusting the pH medium, the surface charges of PDA are controllable. The zeta potential of the Ag/PDA@Ag₂S was determined at various pH values and the results are presented in Figure S6. The isoelectric point (IEP) of the catalyst was found to be 3.78. It is observed that zeta-potential (surface charge of Ag/PDA@Ag₂S) is positive for pH values lower than 3.78 and is negative above that. For example, 80.5 and 72.2% of MB and RB (50 mg/L) are increasingly degraded respectively (Fig. 2a and b) only after 10 minutes while these percentages were less than 5% for both MO and CR (50 mg/

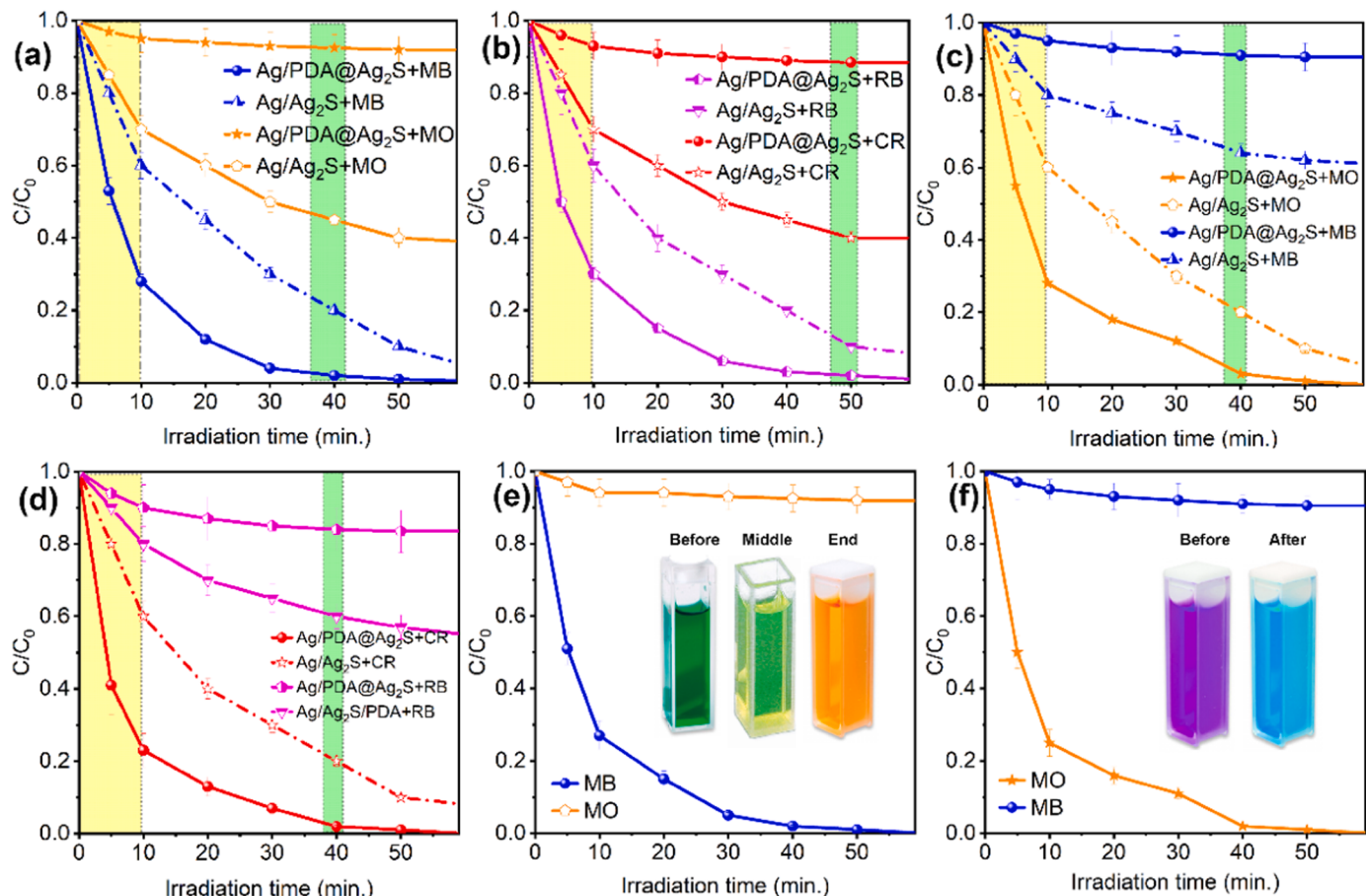


Fig. 2. Separate degradation of (a) MB and MO at pH 10, (b) RB and CR at pH 10, (c) MB and MO at pH 2, (d) RB and CR at pH 2, against pH-responsive Ag/PDA@Ag₂S smart photocatalysts and PDA-free Ag/Ag₂S surface. [condition: 50 mg photocatalyst, 200 mL of a mixture of four cationic and anionic dye solutions 50 mg/L, Tris-buffer buffer solution for pH control, 30 min stirring in dark conditions, illumination (300 W Xe lamp equipped with AM 1.5 filter) at room temperature]. Plots of photodegradation of MB (25 mg/L) and MO (25 mg/L) mixture against Ag/PDA@Ag₂S smart photocatalyst (e) at pH =10 (The inset shows the colour change before, in the middle, and at the end of the reaction, left to right, respectively). (f) The plot of photodegradation of MB (25 mg/L) and MO (25 mg/L) mixture against Ag/PDA@Ag₂S smart photocatalyst at pH= 2 (The inset shows the colour change before and at the end of the reaction, left to right, respectively).

L, Fig. 2a and b) using pH-responsive Ag/PDA@Ag₂S photocatalysts. More interestingly, the photodegradation rate of the cationic dyes was much faster with the Ag/PDA@Ag₂S smart heterojunctions than that of bare Ag/Ag₂S catalyst, indicating the enhanced oxidative strength of the pH-responsive Ag/PDA@Ag₂S smart photocatalysts. The phenomenon is explained by electrostatic attraction and charge repulsion that happened between the PDA shell of the catalyst and the dye charges. It is expected in an acidic medium, the anionic dyes could be degraded faster with higher efficiency by the catalyst due to the positively charged surface of the catalyst at lower pH values than IEP. The results for separate degradation of each dye are given in Fig. 2c and d. Based on the results obtained, to examine further the selectivity of the selective Ag/PDA@Ag₂S heterojunctions photocatalyst and the role of PDA in the composite, a series of reactions were performed for a dye mixture containing MB (25 mg/L) and MO (25 mg/L) at both pH values of 2 and 10.

According to Fig. 2e, ca. 80.0% of MB was degraded after 10 minutes while this value is around 4.0% for MO at the same time at pH 10. These results are also proven visually by the colour change through the photocatalysis processes (see inset). After mixing MB (blue colour) and MO (yellow colour), a green solution was obtained. However, upon irradiation, this colour gradually gets yellowish, and at the end of the reaction, the colour of the mixtures turns completely yellow. This colour change can be rationalised by the removal and decolorization of MB in the mixture and the remaining MO in the mixture. It can be concluded that as-prepared smart photocatalysts can selectively degrade organic dyes.

Likewise, degradation efficiency for a mixture of dyes (MB and MO, 25 mg/L each) was examined at pH=2 and the outcomes are shown in Fig. 2f. It is noted that the pristine MO at pH=2 is red which is different from MO is yellow at pH=10. Hence, the colour of the mixture containing MO (red) and MB (blue) before irradiation is purple. Upon commencing the photocatalytic reaction, this colour turned to average blue which can be interpreted by decolorization of MO over time, the only dye that remained in the solution was MB. A first-order kinetic model was applied for the oxidation assessment of dyes using the catalyst according to Eq.6:

$$\ln\left(\frac{C}{C_0}\right) = -k_{obs.} \cdot t \quad (1)$$

Where C_0 , C , and $k_{obs.}$ (min^{-1}) are initial concentration, dye concentrations at time t , and the apparent reaction rate constant. By comparing the apparent reaction rate constants, it is observed at pH 10, the apparent reaction rate constant for MB degradation ($k_{obs.} = 0.0909 \text{ min}^{-1}$) is 82.6 times higher (faster) than that of MO ($k_{obs.} = 0.0011 \text{ min}^{-1}$). On the other side, at pH 2, the MO degradation is 57.5 times faster than that of MB ($k_{obs. MO} = 0.0874 \text{ min}^{-1}$ vs $k_{obs. MB} = 0.00152 \text{ min}^{-1}$). Table S1 shows a Comparison of the photocatalytic H₂ generation achieved in the presented work with recent results reported in the literature.

3.3. Photocatalytic hydrogen evolution

Fig. 3a illustrates the photocatalytic performance of the Ag/Ag₂S and Ag/PDA@Ag₂S heterojunction photocatalysts in hydrogen evolution under solar simulated irradiation. The hydrogen production over bare Ag/Ag₂S is 36.0 μmol while the Ag/PDA@Ag₂S photocatalysts can generate H₂ with an outstanding enhancement with a rate of 126.9 μmol by the factor of 3.52 times after 4 hrs (31.7 vs 9.0 μmol h⁻¹). PDA was mixed physically and mechanically with Ag₂S/Ag by different ratios and the result is given in Fig. 3b. There is a stark decrease in the H₂ production rate for simple mixing. The obtained value is even less than that of a bare Ag/Ag₂S hybrid catalyst and continues to decrease for higher ratios of PDA. Because PDA alone cannot produce H₂ and in the mixture can probably hinder effective light penetration to Ag/Ag₂S. It can be concluded that PDA was deposited successfully on the Ag₂S surface. It also emphasizes the crucial role of N-containing groups in PDA with intimate interaction with Ag and Ag₂S leading to efficient electron transfer and active sites [1,34].

All these experimental investigations indicate that experimental results are well aligned with the theoretical prediction above, confirming the validation of theoretical models.

3.4. The mechanism underlying such photocatalytic behavior

3.4.1. Optical and photoelectric properties

Optical and electrochemical properties were investigated by UV-Vis and photoluminescence (PL) spectroscopy, photocurrent (PC) measurement, and electrochemical impedance spectroscopy (EIS). The results are given in Fig. 4. Fig. 4a shows diffuse reflectance spectra (DRS) of the Ag/Ag₂S and Ag/PDA@Ag₂S. The light absorption range of photocatalysts after ultrathin layer PDA coating on Ag₂S is slightly expended and its intensity is also increased, which is in good agreement with previous studies [28,35]. The linear sweep voltammetry (LSV) results presented in Fig. 4b indicate the overpotential for Ag/PDA@Ag₂S is much lower than that of Ag/Ag₂S, suggesting that Ag/PDA@Ag₂S presents a better reduction ability. Photocurrent test (Fig. 4c) indicates the better separation of the electrons and holes leading to the enhanced photocatalytic activity of Ag/PDA@Ag₂S smart heterojunction photocatalysts in comparison with bare Ag/Ag₂S. As can be in Fig. 4c, when the visible light turns on, the photocurrent density generated for Ag/PDA@Ag₂S, in the second cycle, is about 2.6 times higher than that of Ag/Ag₂S. Besides, EIS Nyquist plots, given in Fig. 4d, are in accordance with PC result under light illumination, showing that Ag/PDA@Ag₂S with a smaller arc radius in its curve exhibits higher

photocatalytic performance, implying quicker charge carrier transportation and effective separation of the electrons and holes excited in Ag/PDA@Ag₂S. Room temperature PL spectra of Ag/Ag₂S and Ag/PDA@Ag₂S smart photocatalyst are carefully collected for comparison which are illustrated in Fig. 4e. It is observed that Ag/PDA@Ag₂S smart heterojunction photocatalysts show lower radiative intensity, indicating the suppressed combination of photogenerated pairs Ag/PDA@Ag₂S presents higher photocatalytic activity compared to Ag/Ag₂S. These all indicate that PDA can facilitate the charge transfer and inhibit their recombination. To further investigate the separation, relaxation process, and fluorescence lifetime of photoexcited charges, time-resolved photoluminescence spectra (TRPL) were measured. The decay curves were smoothly fitted with a double-exponential equation as shown in Fig. 4f. The average lifetime (τ_a) was calculated according to the following equation and the results are tabulated in Table 1:

$$\tau_a = \frac{A_1 \tau_1^2 + A_2 \tau_2^2}{A_1 \tau_1^2 + A_2 \tau_2^2} \quad (2)$$

where A_1 and A_2 represent the pre-exponential factors and τ_1 and τ_2 are the lifetimes (ns) for the radiative and non-radiative recombination processes, respectively [36].

The fitted decay curves disclose the lifetime (τ) and percentage (Rel. %) of charge carriers (Table 1). The short lifetime (τ_1) corresponds to the radiative recombination of the carriers, while the long lifetime (τ_2) is assigned to the non-radiative recombination and energy-transfer process [37]. It is noted that the unrecombined radiative carriers get involved in surface photocatalytic reactions. Hence, the decrease in τ_1 percentage signifies radiative recombination is inhibited [38]. Photoexcited charge transfer is hence expected to be enhanced as a result of reducing radiative recombination. Likewise, a relatively smaller τ_2 value (and lower percentage) suggests a more efficient nonradiative decay pathway [39]. It is observed in Table 1, that Ag/PDA@Ag₂S shows a lower percentage of τ_1 (69.80%) than Ag/Ag₂S (81.50%), indicating that the radiative recombination over Ag/Ag₂S is hindered upon PDA application as an intermediate layer due to the formation of S-scheme heterojunction [38, 40,41]. The significantly longer average lifetime of Ag/PDA@Ag₂S, suggests higher electron-hole separation through a uniform and ultrathin layer interface introduced by a homogeneous loading of PDA on Ag₂S [42]. It is worth noting that in-situ XPS demonstrates the peaks of Ag 3d of Ag/PDA@Ag₂S shift toward lower energies under UV illumination (Figure S7). This shift indicates the electrons transfer from PDA to Ag₂S after illumination. As shown in Fig. 4g, PDOS studies further strengthen and validate the discussed results. The PDOS was calculated to clarify the electronic structure and characters further. The conduction

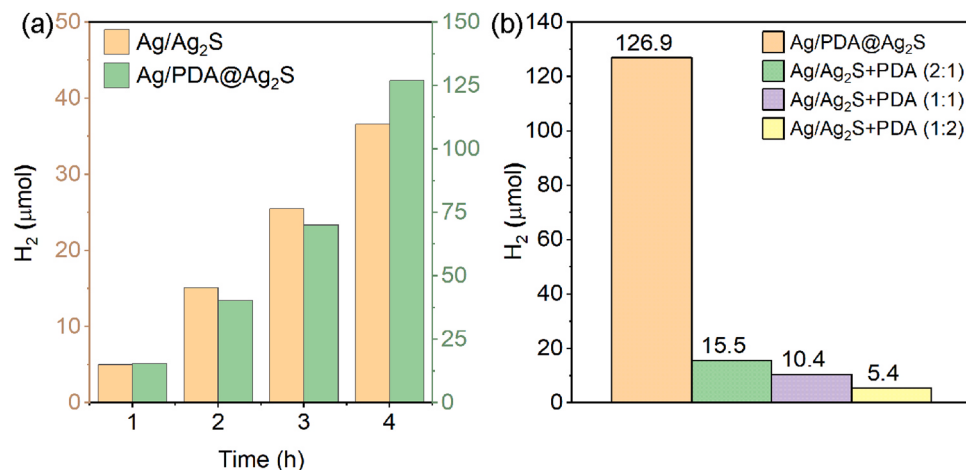


Fig. 3. (a) The photocatalytic H₂-production activity of Ag/Ag₂S and Ag/PDA@Ag₂S at different time intervals (condition: 20 mg of photocatalyst, 40 mL H₂O, 10 mL CH₃OH 20 V/V% as electron donor, 30 min anaerobic condition, light: 300 W Xe lamp equipped with AM 1.5 filter). (b) Comparison of H₂ production activity of Ag/PDA@Ag₂S with Ag/Ag₂S physically mixed with PDA in various ratios after 4 hrs.

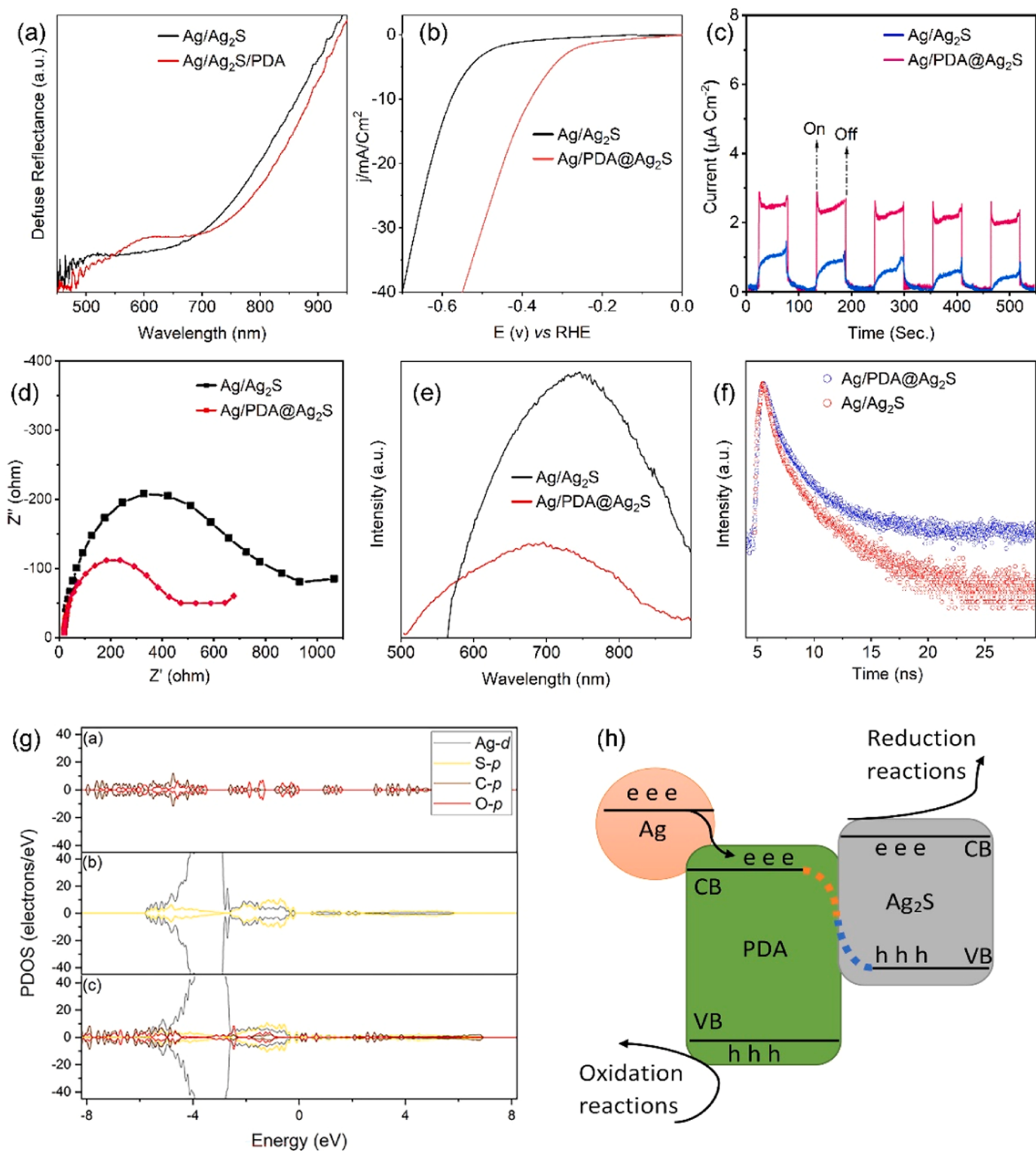


Fig. 4. (a) UV–Vis DRS, (b) LSV curves, (c) PC, and (d) Nyquist plots of the Ag/Ag₂S and Ag/PDA@Ag₂S photocatalysts. The electrochemical system consisted of an FTO glass covered by the photocatalyst, a Pt wire, and a saturated Ag/AgCl/KCl (saturated) electrode as the working, counter, and reference electrode, respectively. A 0.3 mol/L Na₂SO₄ aqueous solution served as the electrolyte. The EIS measurement was conducted with an AC-applied voltage of 5 mV. The EIS of the active material varied between 0.2 to −0.6 V at a potential difference of 20 mV in a staircase behavior. (e) Room-temperature PL at the excitation wavelength of 470 nm; (f) Time-resolved photoluminescence spectra of the Ag/Ag₂S and Ag/PDA@Ag₂S at the excitation wavelength of 405 nm. (g) Calculated projected density of states (PDOS). (a), (b), and (c) are the PDOS of PDA, Ag₂S, and PDA-Ag₂S, respectively. (h) Schematic illustration of possible charge transfer in Ag/PDA@Ag₂S photocatalysts.

Table 1

Double exponential fitted parameters obtained from TRPL spectra.

Sample	τ_1 (ns)	Rel. (%)	τ_2 (ns)	Rel. (%)	τ_a (ns)
Ag/PDA@Ag ₂ S	0.31	68.8	3.8	31.2	3.07
Ag/Ag ₂ S	0.22	81.5	2.3	18.5	1.58

τ_a stands for the average lifetime (ns) of photogenerated carriers; τ_1 and τ_2 represent the lifetime (ns) in the radiative and non-radiative recombination, respectively.

band (CB) of PDA is mainly composed of C *p*-orbital electrons, and the *p*-orbital delocalization is below -3.70 eV (Fig. 4g(a)). Fig. 4g(b) shows a strong peak of Ag₂S *d*-orbital located at the deep inside valence band (VB) around -3.00 eV. Furthermore, Fig. 4g(c) depicts that the CB of PDA down-shifts to encourage electron transportation from PDA to Ag₂S, and the localization of electrons crosses the Fermi level. Moreover, the *p*-orbitals of C and O overlap with the *d*-orbital of Ag at a negative energy range. These results prove the electron transportation and strong interrelation between PDA and Ag₂S. Furthermore, the work function is calculated, which plays a pivotal role in modulating the built-in electric field and the direction of electron flow [43]. As Figure S8 illustrates, the calculated work functions of Ag₂S and PDA are 4.97 and 4.58 eV, respectively. The higher work function of Ag₂S indicates a lower Fermi level than that of PDA, resulting in electron migration from PDA to Ag₂S to achieve equilibrium of Fermi energy levels. Such electron

redistribution induces the built-in electric field formation within the Ag₂S/PDA interface. Under light irradiation, the built-in electric field impedes the reverse movement of photogenerated electrons and holes, enhancing photocatalytic efficiency. Upon excitation, the feasible relaxation pathways for the excited electrons may include (Fig. 4h): (1) Silver, being a metal, has a high density of free electrons in its conduction band. When light interacts with the silver nanoparticles, it induces the excitation of these free electrons, leading to the generation of hot electrons. These hot electrons can then tunnel or transfer across the interface to the conduction band of the adjacent semiconductor, PDA. Once transferred to the conduction band of PDA, the hot electrons can participate in photocatalytic reactions, such as reducing adsorbed species or initiating chemical transformations.; (2) the electrons in CB of PDA recombine with the holes in Ag₂S and emit photons resulting in the PL spectra for both (S-scheme charge transfer); (3) the holes in the VB of PDA and the electrons in the CB of Ag₂S remain unreacted and involve redox reactions.

3.4.2. EPR investigations

3.4.2.1. Photocatalytic H₂ evolution. To further examine the capability of the bare Ag/Ag₂S and Ag/PDA@Ag₂S heterojunction photocatalysts in H₂ production, a series of electron paramagnetic resonance (EPR) tests were performed to monitor hydrogen free radical (H[•]), as an

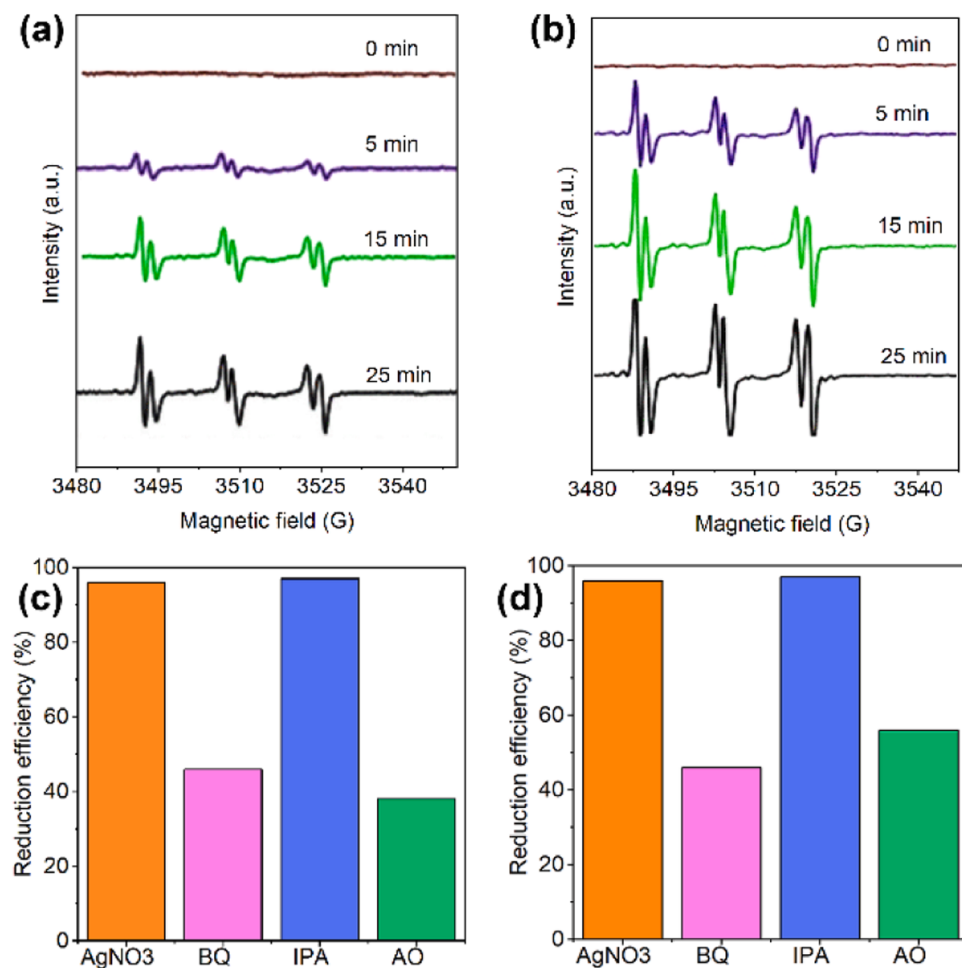


Fig. 5. ESR spectra of POBN-H[•] adduct (a) Ag/Ag₂S, (b) Ag/PDA@Ag₂S smart heterojunction. [2-methyl-N-(4-pyridinylmethylene)-2-propanamine N,N'-dioxide (POBN) was used as a spin trap]. Quenching experiments on (c) MB (50 mg L⁻¹, 200 mL, pH 10) and (d) MO (50 mg L⁻¹, 200 mL, pH 2) by Ag/PDA@Ag₂S smart heterojunction photocatalysts against various scavengers BQ, AO, AgNO₃ or IPA. [Silver nitrate (AgNO₃, 0.02 mol L⁻¹), isopropanol (IPA, 0.02 mol L⁻¹), ammonium oxalate (AO, 0.02 mol L⁻¹), or 4-benzoquinone (BQ, 0.02 mol L⁻¹) was added into the reaction system to identify the reactive species of e⁻, OH, h⁺, and O²⁻, respectively].

intermediate for the photocatalytic H_2 production, during the reaction process [1]. The 2-methyl-N-(4-pyridinylmethylene)-2-propanamine N,N'-dioxide (POBN) spin-trapping ESR spectra for bare Ag/ Ag_2S and Ag/PDA@ Ag_2S hybrid heterojunctions are presented in Fig. 5a and b. It is observed that POBN- H^{\bullet} adduct was detected for these two photocatalysts against irradiation but the amount of H^{\bullet} radical formation is higher at all time intervals. This result is in accordance with all previous characterization results and especially with the H_2 production result.

3.4.2.2. Photocatalytic selective organic dyes oxidation. It has been reported that despite not having the photocatalytic capability, for the degradation of organic dyes, PDA, could enhance remarkably the photocatalytic properties via a synergistic effect with photocatalyst through the presence of the $\pi-\pi^*$ electron transition [44]. For the organic photodegradation mechanism, EPR analyses were again applied to probe and detect reactive oxygen species (ROS) responsible for the degradation processes. A series of quenching experiments were carried out by introducing some scavengers (0.02 mol L⁻¹ each) namely benzoquinone (BQ), isopropyl alcohol (IPA), $AgNO_3$, and ammonium oxalate (AO) to trap $O_2^{\bullet-}$, $^{\bullet}OH$, e^- , and h^+ species, respectively [45]. As observed in Fig. 5c and d, using Ag/PDA@ Ag_2S smart heterojunctions photocatalyst with IPA and $AgNO_3$ as scavengers, the degradation efficiency of MB (at pH 10) did not exhibit obvious reduction, indicating that both $O_2^{\bullet-}$ and h^+ were dominating the degradation process. Likewise, at pH 2, the results showed that the degradation performance of MO declined to 37% or 44% when using AO and BQ, respectively implying again the photodegradation domination process by h^+ and $O_2^{\bullet-}$. It is expected that $^{\bullet}OH$ might not play an important role in photocatalytic degradation in that the VB potential of the Ag/ Ag_2S smart photocatalyst is much less than the value expected to produce $^{\bullet}OH$ (2.8 V vs NHE). Although the introduced PDA layer can usefully accept holes in the valence state from the Ag_2S , at this lowered oxidative potential, Ag/PDA@ Ag_2S cannot generate hydroxyl radicals. Meanwhile, the photogenerated electrons can be captured by the adsorbed molecular oxygen (O_2) leading to superoxide $O_2^{\bullet-}$ radicals.

3.5. Photocatalyst stability study

As explained above, PDA as the interface between Ag and Ag_2S not only constitutes a built-in field facilitating charge separation in the bulk, but also protecting Ag_2S from corrosion, leading to the improvement of both photocatalytic performance and stability of the photocatalyst. What's more, other studies have shown that the photostability of the photocatalysts was enhanced through their surface protection from environmental damages and stoichiometry losses. To consider catalysts potentially for large-scale and industrial applications, it is crucial to probe the stability and reusability of catalysts that were determined by consecutive tests of MB and MO dyes (as representative for cationic and ionic dyes) removal in both pH values of 2 and 10. For each cycle, the catalyst was washed thrice with distilled water, and ethanol and dried in a 40 °C vacuum oven for 7 h. In the solution mixture, the concentration of each dye was 50 mg/L. As observed in Figure S9a and b, the degradation rates of seven cycles declined from 100% to 91% (pH10) and 100–90% (pH 2) for MB and MO, respectively after seven cycles against Ag/PDA@ Ag_2S selective photocatalysts.

Furthermore, Figure S9c-d presents the recycling tests of the bare Ag/ Ag_2S and Ag/PDA@ Ag_2S . While those reduction values are remarkably higher for bare Ag- Ag_2S that might correspond to (i) probable leaching of Ag NPs on the surface of Ag_2S substrate due to the mechanical agitation in the reacted process; (ii) A part of Ag- Ag_2S reaction sites of the catalyst were occupied by dyes and were not renewable. This means PDA can hold Ag NPs strongly and prevent leaching and active site deactivation by acting as an interface to collect radical species on its surface and react with organic dyes. As observed, when using Ag/PDA@ Ag_2S as photocatalysts, within 4 hours, it can produce

H_2 around 115 μ mol (28.75 μ mol h⁻¹) after 16 cycles (less than 10% reduction) while that amount is ca. 15 μ mol (3.75 μ mol h⁻¹) indicating about 60% lower performance for Ag/ Ag_2S . It is concluded that the presence of PDA as the shell on the Ag_2S catalyst surface not only improves the photocatalytic activity by facilitating charge separation but also boosts remarkably its photocatalytic stability by preventing Ag NPs from leaching corrosion and mechanical defects as well. Furthermore, by comparing the XRD spectra of the photocatalyst before and after the fifth cycle in Figure S10, there is no touchable change in XRD spectra further indicating the stability of the smart photocatalyst. To further evaluate the microstructure stability of the photocatalyst, SEM images were collected after the photocatalyst reaction and presented in Figure S11. As can be seen, in the images, Ag nanoparticles consistently remained on the surface Ag_2S /PDA indicating the stability of the microstructure of the photocatalyst.

4. Conclusion

We have successfully fabricated Ag/PDA@ Ag_2S smart heterojunction photocatalysts via a facile, fast, and in-situ polymerization method with a precise and ultra-thin layer of PDA on an Ag_2S surface. We found that PDA, as an interface, can improve the photocatalytic property of the Ag/ Ag_2S hybrid photocatalysts. The introduced PDA ultra-thin layer shell not only helps with charge transport and separation processes but also increases the photostability of the Ag_2S /Ag photocatalyst especially in the hydrogen evolution process by preventing the photocatalyst from photo-corrosion and Ag leaching on the Ag_2S surface. The PDA endows a new function that Ag/ Ag_2S hybrid photocatalyst can be switched on and off by adjusting the pH or ionic strength of the reaction medium leading to a selective photodegradation of mixed organic dyes. Such an innovative heterojunction thus assures visible-light absorption, boosts charge separation, and increases the redox ability of charge carriers simultaneously. Besides the matched band structures of the two semiconductors (PDA and Ag_2S), an intimate and strong interfacial contact of them is of vital importance to promote the S-scheme charge transfer path across the interface of the heterojunction.

CRediT authorship contribution statement

Farzin Nekouei: Writing – review & editing, Writing – original draft, Supervision, Project administration, Methodology, Investigation, Formal analysis, Data curation, Conceptualization. **Tianyi Wang:** Writing – review & editing, Software, Investigation, Formal analysis. **Farzaneh Keshtpour:** Methodology, Investigation, Formal analysis. **Yun Liu:** Writing – review & editing. **Hao Li:** Writing – review & editing, Software, Methodology, Formal analysis. **Shahram Nekouei:** Writing – review & editing, Methodology, Investigation, Formal analysis, Data curation, Conceptualization.

Declaration of Competing Interest

The authors declare that they have no known competing financial interests or personal relationships that could have appeared to influence the work reported in this paper.

Data Availability

Data will be made available on request.

Acknowledgment

We acknowledge the Center for Computational Materials Science, Institute for Materials Research, Tohoku University for the use of MASAMUNE-IMR (202212-SCKXX-0204) and the Institute for Solid State Physics (ISSP) at the University of Tokyo for the use of their supercomputers. T. W. acknowledges the JSPS KAKENHI (No.

JP23KF0102). The authors also acknowledge Beijing PARATERA Tech Co., Ltd. and the National Computational Infrastructure (NCI) for providing computational resources.

Appendix A. Supporting information

Supplementary data associated with this article can be found in the online version at [doi:10.1016/j.apcatb.2024.123974](https://doi.org/10.1016/j.apcatb.2024.123974).

References

- [1] F. Nekouei, S. Nekouei, M. Pouzesh, Y. Liu, Porous-CdS/Cu2O/graphitic-C3N4 dual p-n junctions as highly efficient photo/catalysts for degrading ciprofloxacin and generating hydrogen using solar energy, *Chem. Eng. J.* 385 (2020) 123710.
- [2] S. Nekouei, F. Nekouei, Photocatalytic degradation of norfloxacin and its intermediate degradation products using nitrogen-doped activated carbon-CuS nanocomposite assisted by visible irradiation, *Appl. Organomet. Chem.* 32 (2018) e4418.
- [3] F. Nekouei, X. Wen, Z. Zheng, Q. Sun, T. Lu, H. Orton, F. Kremer, S. Nekouei, T. Yuan, E.H. Abdelkader, B. Liu, A. Tricoli, G. Otting, Z. Liu, T. Frankcombe, Y. Liu, InOOH-mediated intergrown heterojunctions for enhanced photocatalytic Performance: Assembly and interfacial charge carrier transferring, *Chem. Eng. J.* 442 (2022) 136355.
- [4] Q. Wang, K. Domen, Particulate photocatalysts for light-driven water splitting: mechanisms, challenges, and design strategies, *Chem. Rev.* 120 (2019) 919–985.
- [5] C. Zhang, C. Xie, Y. Gao, X. Tao, C. Ding, F. Fan, H.L. Jiang, Charge separation by creating band bending in metal–organic frameworks for improved photocatalytic hydrogen evolution, *Angew. Chem. Int. Ed.* 61 (2022) e202204108.
- [6] G. Xu, H. Zhang, J. Wei, H.-X. Zhang, X. Wu, Y. Li, C. Li, J. Zhang, J. Ye, Integrating the g-C3N4 nanosheet with B–H bonding decorated metal–organic framework for CO2 activation and photoreduction, *ACS Nano* 12 (2018) 5333–5340.
- [7] Z. Lin, C. Du, B. Yan, C. Wang, G. Yang, Two-dimensional amorphous NiO as a plasmonic photocatalyst for solar H2 evolution, *Nat. Commun.* 9 (2018) 4036.
- [8] F. Nekouei, S. Nekouei, Determination of copper, nickel and cobalt in water and food samples by FAAS after separation and preconcentration using multi walled carbon nanotubes modified by methyl-(2-pyridyl) ketone oxime, *Indian J. Sci. Res.* 8 (2014) 138–145.
- [9] S. Nekouei, F. Nekouei, Photocatalytic degradation of norfloxacin and its intermediate degradation products using nitrogen-doped activated carbon-CuS nanocomposite assisted by visible irradiation, *Appl. Organomet. Chem.* 32 (2018) e4418.
- [10] H. Zhou, M. Wang, F. Kong, Z. Chen, Z. Dou, F. Wang, Facet-dependent electron transfer regulates photocatalytic valorization of biopolymers, *J. Am. Chem. Soc.* 144 (2022) 21224–21231.
- [11] R.T. Tung, Recent advances in Schottky barrier concepts, *Mater. Sci. Eng.: R: Rep.* 35 (2001) 1–138.
- [12] M.M. Shahjamali, Y. Zhou, N. Zaraee, C. Xue, J. Wu, N. Large, C.M. McGuirk, F. Boey, V. Dravid, Z. Cui, G.C. Schatz, C.A. Mirkin, Ag–Ag2S hybrid nanoprisms: structural versus plasmonic evolution, *ACS Nano* 10 (2016) 5362–5373.
- [13] H. Yu, W. Liu, X. Wang, F. Wang, Promoting the interfacial H2-evolution reaction of metallic Ag by Ag2S cocatalyst: a case study of TiO2/Ag–Ag2S photocatalyst, *Appl. Catal. B: Environ.* 225 (2018) 415–423.
- [14] W. Yang, L. Zhang, Y. Hu, Y. Zhong, H.B. Wu, X.W. Lou, Microwave-assisted synthesis of porous Ag2S–Ag hybrid nanotubes with high visible-light photocatalytic activity, *Angew. Chem. Int. Ed.* 51 (2012) 11501–11504.
- [15] G. Hodes, J. Manassen, D. Cahen, Photoelectrochemical energy conversion and storage using polycrystalline chalcogenide electrodes, *Nature* 261 (1976) 403–404.
- [16] N. Zhao, J. Vickery, G. Guerin, J.I. Park, M.A. Winnik, E. Kumacheva, Self-assembly of single-tip metal–semiconductor nanorods in selective solvents, *Angew. Chem.* 123 (2011) 4702–4706.
- [17] G. Hong, J.T. Robinson, Y. Zhang, S. Diao, A.L. Antaris, Q. Wang, H. Dai, In vivo fluorescence imaging with Ag2S quantum dots in the second near-infrared region, *Angew. Chem. Int. Ed.* 51 (2012) 9818–9821.
- [18] T. Liu, B. Liu, L. Yang, X. Ma, H. Li, S. Yin, T. Sato, T. Sekino, Y. Wang, RGO/Ag2S/TiO2 ternary heterojunctions with highly enhanced UV-NIR photocatalytic activity and stability, *Appl. Catal. B: Environ.* 204 (2017) 593–601.
- [19] R. Li, J. Hu, M. Deng, H. Wang, X. Wang, Y. Hu, H.-L. Jiang, J. Jiang, Q. Zhang, Y. Xie, Integration of an inorganic semiconductor with a metal–organic framework: a platform for enhanced gaseous photocatalytic reactions, *Adv. Mater.* 26 (2014) 4783–4788.
- [20] M. Fahlman, S. Fabiano, V. Gueskine, D. Simon, M. Berggren, X. Crispin, Interfaces in organic electronics, *Nat. Rev. Mater.* 4 (2019) 627–650.
- [21] G. Kresse, J. Furthmüller, Vienna ab-initio simulation package (VASP), Institut für Materialphysik, Vienna, (2004).
- [22] J.P. Perdew, A. Ruzsinszky, G.I. Csonka, O.A. Vydrov, G.E. Scuseria, L. A. Constantin, X. Zhou, K. Burke, Restoring the density-gradient expansion for exchange in solids and surfaces, *Phys. Rev. Lett.* 100 (2008) 136406.
- [23] P.E. Blöchl, Projector augmented-wave method, *Phys. Rev. B* 50 (1994) 17953.
- [24] W. Kohn, L.J. Sham, Self-consistent equations including exchange and correlation effects, *Phys. Rev.* 140 (1965) A1133.
- [25] H.J. Monkhorst, J.D. Pack, Special points for Brillouin-zone integrations, *Phys. Rev. B* 13 (1976) 5188.
- [26] D. Cheng, X. Bai, J. Pan, J. Wu, J. Ran, G. Cai, X. Wang, In situ hydrothermal growth of Cu NPs on knitted fabrics through polydopamine templates for heating and sensing, *Chem. Eng. J.* 382 (2020) 123036.
- [27] F. Nekouei, Simultaneous cloud point extraction and ion association system for preconcentration of cadmium (II) in the presence of zwitterionic surfactant 3-[(3-cholamidopropyl)-dimethylammonium]-1-propanesulphonate as a chelating agent prior to its spectrophotometric determination, *Indian J. Sci. Res.* 8 (2014) 130–137.
- [28] Y. Kim, E. Coy, H. Kim, R. Mrówczyński, P. Torruella, D.-W. Jeong, K.S. Choi, J. H. Jang, M.Y. Song, D.-J. Jang, Efficient photocatalytic production of hydrogen by exploiting the polydopamine-semiconductor interface, *Appl. Catal. B: Environ.* 280 (2021) 119423.
- [29] F. Chen, W. Yu, Y. Qie, L. Zhao, H. Zhang, L.-H. Guo, Enhanced photocatalytic removal of hexavalent chromium through localized electrons in polydopamine-modified TiO2 under visible irradiation, *Chem. Eng. J.* 373 (2019) 58–67.
- [30] F. Nekouei, S. Nekouei, H. Noorizadeh, Enhanced adsorption and catalytic oxidation of ciprofloxacin by an Ag/AgCl@N-doped activated carbon composite, *J. Phys. Chem. Solids* 114 (2018) 36–44.
- [31] M. Pang, J. Hu, H.C. Zeng, Synthesis, morphological control, and antibacterial properties of hollow/solid Ag2S/Ag heterodimers, *J. Am. Chem. Soc.* 132 (2010) 10771–10785.
- [32] Z. Yang, Y. Wu, J. Wang, B. Cao, C.Y. Tang, In situ reduction of silver by polydopamine: A novel antimicrobial modification of a thin-film composite polyamide membrane, *Environ. Sci. Technol.* 50 (2016) 9543–9550.
- [33] B. Fei, B. Qian, Z. Yang, R. Wang, W. Liu, C. Mak, J.H. Xin, Coating carbon nanotubes by spontaneous oxidative polymerization of dopamine, *Carbon* 46 (2008) 1795–1797.
- [34] F. Nekouei, S. Nekouei, O. Jashnsaz, M. Pouzesh, Green approach for in-situ growth of highly-ordered 3D flower-like CuS hollow nanospheres decorated on nitrogen and sulfur co-doped graphene bionanocomposite with enhanced peroxidase-like catalytic activity performance for colorimetric biosensing of glucose, *Mater. Sci. Eng.: C* 90 (2018) 576–588.
- [35] Q. Lin, Y. Yang, Y. Ma, R. Zhang, J. Wang, X. Chen, Z. Shao, Bandgap engineered polyppore–polydopamine hybrid with intrinsic Raman and photoacoustic imaging contrasts, *Nano Lett.* 18 (2018) 7485–7493.
- [36] B. He, C. Bie, X. Fei, B. Cheng, J. Yu, W. Ho, A.A. Al-Ghamdi, S. Wagh, Enhancement in the photocatalytic H2 production activity of CdS NRs by Ag2S and NiS dual cocatalysts, *Appl. Catal. B: Environ.* 288 (2021) 119944.
- [37] K. Das, S.N. Sharma, M. Kumar, S.K. De, Morphology Dependent Luminescence Properties of Co Doped TiO2 Nanostructures, *J. Phys. Chem. C* 113 (2009) 14783–14792.
- [38] F. Xu, K. Meng, B. Cheng, S. Wang, J. Xu, J. Yu, Unique S-scheme heterojunctions in self-assembled TiO2/CsPbBr3 hybrids for CO2 photoreduction, *Nat. Commun.* 11 (2020) 1–9.
- [39] W.-J. Ong, L.K. Putri, Y.-C. Tan, L.-L. Tan, N. Li, Y.H. Ng, X. Wen, S.-P. Chai, Unravelling charge carrier dynamics in protonated g-C3N4 interfaced with carbon nanodots as co-catalysts toward enhanced photocatalytic CO2 reduction: a combined experimental and first-principles DFT study, *Nano Res.* 10 (2017) 1673–1696.
- [40] P. Xia, B. Zhu, J. Yu, S. Cao, M. Jaroniec, Ultra-thin nanosheet assemblies of graphitic carbon nitride for enhanced photocatalytic CO2 reduction, *J. Mater. Chem. A* 5 (2017) 3230–3238.
- [41] A. Meng, B. Cheng, H. Tan, J. Fan, C. Su, J. Yu, TiO2/polydopamine S-scheme heterojunction photocatalyst with enhanced CO2-reduction selectivity, *Appl. Catal. B: Environ.* 289 (2021) 120039.
- [42] X. Shi, S. Kim, M. Fujitsuka, T. Majima, In situ observation of NiS nanoparticles depositing on single TiO2 mesocrystal for enhanced photocatalytic hydrogen evolution activity, *Appl. Catal. B: Environ.* 254 (2019) 594–600.
- [43] Y. Lu, X. Jia, Z. Ma, Y. Li, S. Yue, X. Liu, J. Zhang, W5+-W5+ pair Induced LSPR of W18O49 to sensitize ZnIn2S4 for full-spectrum solar-light-driven photocatalytic hydrogen evolution, *Adv. Funct. Mater.* 32 (2022) 2203638.
- [44] Y. Liu, K. Ai, L. Lu, Polydopamine and its derivative materials: synthesis and promising applications in energy, environmental, and biomedical fields, *Chem. Rev.* 114 (2014) 5057–5115.
- [45] S. Li, J. Chen, W. Jiang, Y. Liu, Y. Ge, J. Liu, Facile construction of flower-like bismuth oxybromide/bismuth oxide formate pn heterojunctions with significantly enhanced photocatalytic performance under visible light, *J. Colloid Interface Sci.* 548 (2019) 12–19.